Tectonics

RESEARCH ARTICLE
10.1029/2018TC005261

Analogue Modeling of Plate Rotation Effects in Transform Margins and Rift-Transform Intersections

G.-P. Farangitakis[1], D. Sokoutis[2,3], K. J. W. McCaffrey[1], E. Willingshofer[2], L. M. Kalnins[4], J. J. J. Phethean[1], J. van Hunen[1], and V. van Steen[2]

[1]Department of Earth Sciences, Durham University, Durham, UK, [2]Department of Earth Sciences, Utrecht University, Utrecht, the Netherlands, [3]Department of Geosciences, University of Oslo, Oslo, Norway, [4]School of GeoSciences, University of Edinburgh, Edinburgh, UK

Key Points:
- We use analogue models to study transtension and transpression on transform margins and rift-transform intersections due to plate rotation
- The extent and topography of the structures created are strongly dependent on the relative velocity between transform margins
- Our results show good agreement with natural examples from the Gulf of California and the Tanzania Coastal Basin

Supporting Information:
- Supporting Information S1

Correspondence to:
G.-P. Farangitakis,
georgios-pavlos.farangitakis@durham.ac.uk

Citation:
Farangitakis, G.-P., Sokoutis, D., McCaffrey, K. J. W., Willingshofer, E., Kalnins, L. M., Phethean, J. J. J., et al. (2019). Analogue modeling of plate rotation effects in transform margins and rift-transform intersections. *Tectonics*, *38*, 823–841. https://doi.org/10.1029/2018TC005261

Received 30 JUL 2018
Accepted 24 JAN 2019
Accepted article online 29 JAN 2019
Published online 2 MAR 2019

Abstract Transform margins are first-order tectonic features that accommodate oceanic spreading. Uncertainties remain about their evolution, genetic relationship to oceanic spreading, and general structural character. When the relative motion of the plates changes during the margin evolution, further structural complexity is added. This work investigates the evolution of transform margins and associated rift-transform intersections, using an analogue modeling approach that simulates changing plate motions. We investigate the effects of different crustal rheologies by using either (a) a two-layer brittle-ductile configuration to simulate upper and lower continental crust, or (b) a single layer brittle configuration to simulate oceanic crust. The modeled rifting is initially orthogonal, followed by an imposed plate vector change of 7° that results in oblique rifting and plate overlap (transpression) or underlap (transtension) along each transform margin. This oblique deformation reactivates and overprints earlier orthogonal structures and is representative of natural examples. We find that (a) a transtensional shift in the plate direction produces a large strike-slip principal displacement zone, accompanied by en-echelon oblique-normal faults that accommodate the horizontal displacement until the new plate motion vector is stabilized, while (b) a transpressional shift produces compressional structures such as thrust fronts in a triangular zone in the area of overlap. These observations are in good agreement with natural examples from the Gulf of California (transtensional) and Tanzania Coastal Basin (transpressional) shear margins and illustrate that when these deformation patterns are present, a component of plate vector change should be considered in the evolution of transform margins.

Plain Language Summary Tectonic plate boundaries on our planet are categorized by their relative motion with respect to each other. The three main categories are those moving away, toward, and parallel to one another. We study the processes occurring when two tectonic plates moving parallel begin to rotate and move away or toward each other. Currently, this is occurring in the Gulf of California, and in the past, it occurred in areas such as the Southern Atlantic, creating the segmented pattern along its midocean ridge. To study these tectonic plate boundaries, we use sandbox modeling. We make miniature models of the Earth's crust with silicone putty and sand and recreate the same movements that tectonic plates go through. This allows us to understand the structures created in such environments better. The pattern and the height or depth of these structures are related to how fast the plates move. This work can help recognize areas where similar deformation has occurred in the past, which is important for hydrocarbon exploration. It can also assist with geothermal energy exploration, as areas where plates move parallel and away from each other present good opportunities for hotter temperatures in the subsurface.

1. Introduction

Transform margins and oblique rifts are first-order structural features present in almost every tectonic plate across the globe. Transform continental margins, in particular, represent 16% of the cumulative length of continental margins (Basile, 2015; Mercier de Lépinay et al., 2016) and accommodate or have accommodated oceanic spreading motion. These features were first discussed and described in the context of shear margins in the 1960–1970s (e.g., Le Pichon & Hayes, 1971; Mascle, 1976; Scrutton, 1979; Turcotte, 1974; Wilson, 1965). Studies in the past three decades have provided improved conceptual models for the evolution of these margins (e.g., Basile, 2015; Basile & Brun, 1999; Bird, 2001; Lorenzo, 1997;

Mercier de Lépinay et al., 2016; Reid & Jackson, 1997). However, transform margins remain considerably less studied than their continental divergent and convergent counterparts. Studies of these margins across the world such as Vøring (Talwani & Eldholm, 1973), Gulf of Aden (Autin et al., 2013; Leroy et al., 2012), India-Arabia plate boundary (Rodriguez et al., 2016), and West Greenland (Peace et al., 2017) suggest that they have a genetic relationship with preexisting structures or anisotropy in the crust (or even the mantle). However, Basile (2015) argues that there are two types of transforms: (a) transform faults that first form in continental lithosphere and may reactivate or cross-cut preexisting structural features (e.g., the Equatorial Atlantic) and (b) transform faults that form after the initiation of oceanic accretion to connect propagating oceanic spreading axes (e.g., the Woodlark Basin; Gerya, 2012) that display little or no inheritance. Bellahsen et al. (2013) proposes a similar classification: Type 1 that form synchronously with the syn-rift structures, Type 2 that form during the continent-ocean transform, and Type 3 that form within the oceanic domain, after the onset of oceanic spreading. Moreover, transform margins are areas of active hydrocarbon exploration with significant exploration risk factors such as uncertainty over the postbreakup uplift patterns in space and time, poor knowledge of structural architecture and associated topography, and diachronous timing of the transform fault activity (Nemcok et al., 2016).

In this study, we focus on examples where plate boundary reorganizations or changes in extension direction or rate have impacted a transform system. This is the case in the Gulf of California (GoC), where a change in extension direction between the Pacific and North American plates has resulted in a large transtensional zone of oblique slip faults and sigmoidal horsetail splays, particularly in the north (e.g., Lizarralde et al., 2007; Persaud et al., 2017; Seiler et al., 2009). West of Madagascar, a plate rearrangement led to the formation of the Davie Fracture Zone (DFZ) in the Tanzania Coastal Basin (TCB), overprinting the preexisting spreading center and fracture zones (Phethean et al., 2016). In Western Australia and the Jan Mayen Ridge near Greenland, changes in extension direction may have resulted in the formation of free-moving microcontinents (e.g., Heine et al., 2002; Schiffer et al., 2018; Stagg et al., 2004; Whittaker et al., 2016). Finally, Davison et al. (2016) suggest the existence of conjugate zones of compressional deformation along the Romanche Fracture Zone.

Dauteuil and Brun (1993) presented the first analogue modeling experiment of oblique rifting or transform margins, investigating the Mohns and Reykjanes ridges in the N. Atlantic to identify segments of oblique transfer zones between the rift segments. Basile and Brun (1999) then used a Riedel box with a brittle-ductile configuration to produce transtensional faulting patterns in continent-ocean transforms and pull-apart basins. Acocella et al. (1999) showed how orientation, geometry, and kinematics of transfer zones depend upon preexisting basement anisotropies, while Dauteuil et al. (2002) tested the influence of lithosphere strength on the development of deformation above a transform boundary. They concluded that major transform faults associated with fast-spreading ridges are formed by diffuse, complex arrays of strike-slip segments, while transform faults associated with slow-spreading ridges form deep, narrow linear valleys. Autin et al. (2013) used a four-layer brittle/ductile/brittle/ductile model of the Gulf of Aden to investigate how inherited basins could partly control present-day geometry of an oblique rift and localization of fracture zones. Philippon et al. (2015) investigated the relation between dip-slip and strike-slip displacements along orthogonal and oblique faults in relation to extension direction. Finally, Zwaan and Schreurs (2017) tested the effects of oblique extension and inherited structural offsets on continental rift interaction and linkage. Experiments with temperature-dependent materials include the work of Grokholskii and Dubinin (2006) and Dubinin et al. (2018), who used heat and a mix of paraffins in their models to replicate the structures created in rifts.

In this work, we report the results of a series of analogue experiments designed to investigate the role that small changes in relative plate motions play in the evolution of transform faults and of strike-slip plate boundaries more generally. We introduce a sequential three-step experiment where (a) orthogonal motion, (b) a rotation, and then (c) oblique motion are imposed on an initially orthogonal rift. This mimics the effect of a change in spreading direction due to a change in the relative Euler pole between the plates and leads to an oblique rift and accompanying transtensional and transpressional zones on the lateral margins. Observations are compared to seismic reflection images from two different margins: the transtensional GoC partitioned oblique margin and the transpressional TCB offshore East Africa (Figure 1).

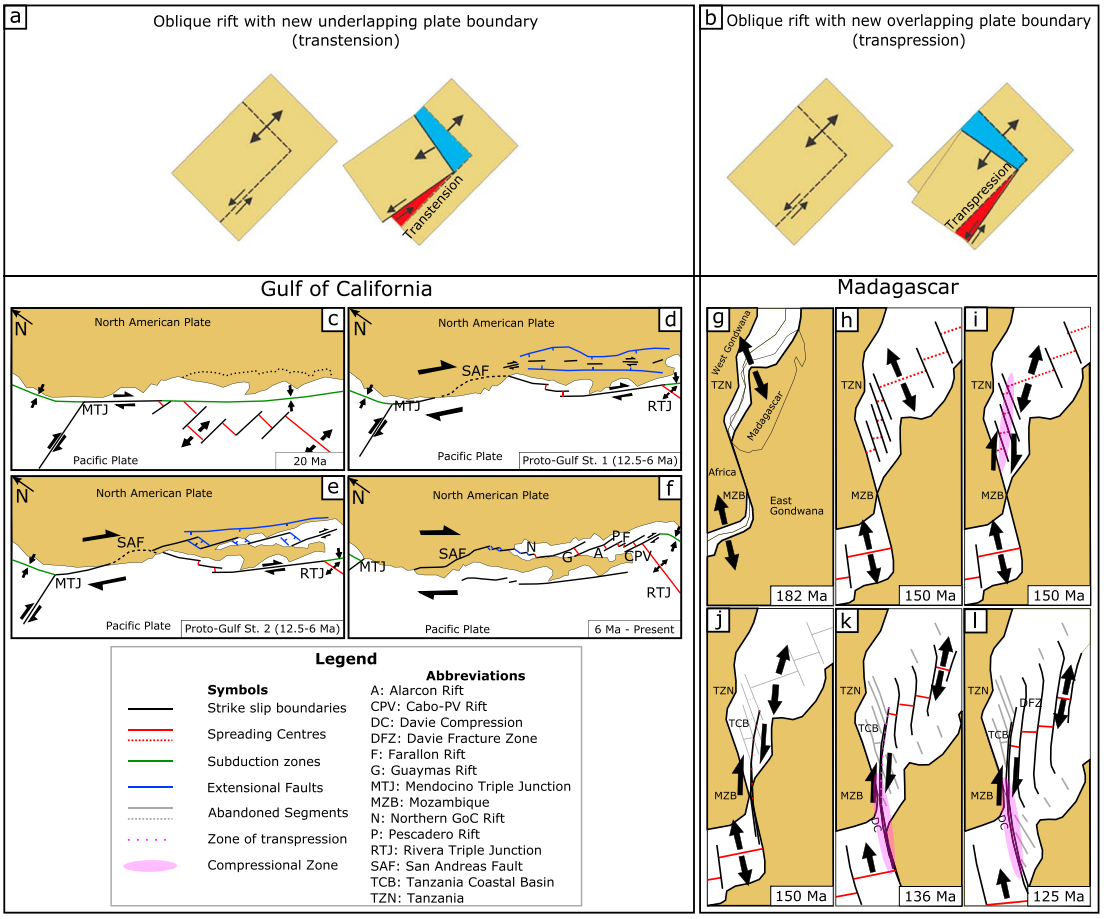

Figure 1. Schematic interpretation of the evolution of (a) a transtensional margin and (b) a transpressional margin. (c–f) Evolution of the Gulf of California from 20 Ma to present (modified from Bennett et al., 2013). (g)–(l) Evolution of the Tanzania Coastal Basin between 182 and 125 Ma (Phethean et al., 2016; Reeves et al., 2016; Tuck-Martin et al., 2018).

2. Geological Background

The GoC is an early stage transform margin, with seafloor spreading in the southern and central Gulf (Lizarralde et al., 2007) and rifting (with potential continental break-up) in the north (Martín-Barajas et al., 2013). Dextral transform motion between the Pacific and North American plates began ~20 Ma (Figure 1c; Atwater & Stock, 1998; Axen, 1995; Bennett et al., 2013; Lonsdale, 1989), with extension in the Proto-Gulf of California beginning ~12 Ma (Figure 1d; Bennett et al., 2013; Persaud et al., 2003). Bennett and Oskin (2014) suggest that a 15° clockwise rotation in the relative motion between the plates at ~8 Ma increased the rift obliquity and favored the development of strike-slip faulting. Shearing localized in en-echelon strike-slip shear zones, which developed into nascent pull-apart basins by 6 Ma (Figure 1e; Bennett et al., 2013) and then into a series of long dextral transform faults connected by smaller rift basins (Figure 1f; Lizarralde et al., 2007; Persaud et al., 2003).

In the northern GoC, the nature and timing of continental rupture are still uncertain, with the presence of oceanic crust suggested in some basins (González-Escobar et al., 2014; Martín-Barajas et al., 2013) and delayed rupture suggested for others (Lizarralde et al., 2007; Martín-Barajas et al., 2013). Deformation in the north is distributed across a pull-apart structure between the Cerro Prieto Fault and the Ballenas Transfrom Fault Zone (Figure 7a; Persaud et al., 2017). This deformation migrated north from the Tiburon Basin ~3.5–2 Ma following a plate reorganization (Seiler et al., 2009). The Cerro Prieto Fault and Ballenas Transfrom Fault Zone strike 6–7° more northerly (312°) than the transforms in the south (305°; Lonsdale, 1989). Dorsey and Umhoefer (2011) and van Wijk et al. (2017) argue that this increased

obliquity contributes to the basin development and late or absent rupture, although initial fault geometries, thick sedimentation, and changing loci of extension may also be factors.

The N-S trending DFZ (Figure 1l) in the TCB is a fossil transform fault that guided the southward drift of East Gondwana (Antarctica, Australia, India, and Madagascar) away from West Gondwana (Africa and South America) during the Jurassic and Early Cretaceous (e.g., Coffin & Rabinowitz, 1987). Following continental breakup at approximately 170 Ma (Geiger et al., 2004), an initial phase of NNW-SSE plate separation resulted in the development of NNW-SSE trending oceanic fracture zones offshore Tanzania (Figures 1g and 1h; e.g., Davis et al., 2016; Phethean et al., 2016; Sauter et al., 2016; Tuck-Martin et al., 2018). By about 150 Ma, the strong continental cores of East and West Gondwana were no longer juxtaposed. Together with the alignment of spreading segments to the north, this created an approximately N-S band of weaker lithosphere. This alignment coincided with a change in plate motion, resulting in N-S separation of East and West Gondwana (Figure 1i; e.g., Davis et al., 2016; Phethean et al., 2016; Sauter et al., 2016). This change in plate motion was incompatible with the NNW-SSE trending fracture zones offshore Tanzania, resulting in transpressional deformation along these structures. Recent work shows evidence of intraplate deformation of the oceanic crust within the TCB adjacent to the DFZ. Sauter et al. (2018) describe buckle folding and thrusting in deformation corridors interpreted as preexisting oceanic fracture zone fabric. This transpressional event was most likely ended by the development of the DFZ, which then accommodated N-S spreading (Figures 1j–1l; Phethean et al., 2016; Reeves et al., 2016).

These two cases of transtension (GoC) and transpression (TCB) provide ideal natural examples to test our analogue modeling experimental approach. In turn, our models can provide insight into the structural evolution of margins such as these and the complexity that may arise.

3. Methodology

3.1. General Definition of the Models

We use a modified experimental array based on Basile and Brun (1999), which comprises a moving plate sliding underneath a brittle/ductile layer configuration that creates preimposed velocity discontinuities (VDs). In this approach, deformation is driven entirely by externally applied boundary conditions (Schellart & Strak, 2016), with preimposed VDs, similar to those in Allemand and Brun (1991) and Tron and Brun (1991). We also use a similar brittle to ductile ratio (2:1, to simulate continental crust) and imposed extension velocity (5 to 10 cm/hr). To simulate similar processes in oceanic crust, we also use a brittle-only configuration (Burov, 2011).

Following an initial orthogonal extension phase, we introduce a rotation of 7°, consistent with the amount of rotation observed in natural examples: Lonsdale (1989) and Bennett et al. (2016) report evidence of ~7–15° of rotation in the GoC from ~6.5 Ma. In Madagascar, the reconstruction in Figures 1c–1h shows ~10° of rotation. Mauduit and Dauteuil (1996) also report a series of transform zones in the Pacific and Atlantic with obliquities ranging between 3° and 8°. Finally, Whittaker et al. (2016) report up to 10° rotation in the Exmouth Plateau in W. Australia.

The brittle/ductile experiments were performed at 5 and 10 cm/hr to explore the influence of velocity and, through it, brittle-ductile layer coupling, with increased velocity corresponding to stronger coupling. This difference in pulling velocity also creates different crustal rheologies in the models (Brun, 2002). The strain rate in the ductile layer increases with increased pulling velocity, leading to more uniform behavior between the ductile and brittle layers. The layer is non-Newtonian, so the increased strain rate corresponds to an increase in apparent viscosity, making the brittle and ductile layers more similar in strength (Figures 3a and 1b). This translates to more distributed strain and the formation of more diffuse structures. In contrast, the brittle experiment corresponding to oceanic crust is independent of velocity , and thus strain rate (Table 1 and Figure 3c). Topography changes in the models are mapped using a laser scanner at discrete intervals. Finally, we use a small funnel to manually add alternating color layers of feldspar sand in the topographic lows (and thrust fronts). This is done every 2–3 min after checking that new structural features have been created. These layers act as syn-rift sedimentation (and in the case of thrusts as an extra protective layer) and facilitate observations of deformation when the models are cut to produce cross sections. At the end of each experiment run, the model is also covered with a thick protective layer of black and white sand for the wetting and cutting process.

Table 1
Model parameters

Experiment number	Model type	Brittle layer thickness (cm)	Ductile layer thickness (cm)	Extension velocity (cm/hr)	Total extension (cm)	Rotation angle (°)	Scaled thickness (km)	Scaled velocity (cm/yr)
1	Brittle/ductile	1.6	0.8	5	7	7	14.4–24 (continental)	~2.5 (range: 1.5–5)
2	Brittle/ductile	1.6	0.8	10	7.2	7	14.4–24 continental)	~5 (range: 3.1–10)
3	Brittle Only	4	—	Strain rate independent	7	7	4–5 (oceanic)	Velocity independent

3.2. Kinematic Set-up

The model configuration (Figure 2) allows us to simultaneously investigate both overlap and underlap caused by the rotation of the moving plate on parallel strike-slip boundaries. The rotating plate is represented by a 60 × 30 cm plastic plate underneath the silicone putty/feldspar sand layers. At the trailing edge of the plastic plate, a second plastic sheet is fixed above the moving plate and acts as a VD imposing a rift (Figure 2). The moving plate is guided by a series of metal bars at the front and rear of the model. These (a) guide the plate to move straight and then rotate and (b) do not allow it to rotate more than 7°. Two heavy metal blocks act as a mechanical elbow (Figure 2, yellow boxes), forcing the plate to rotate until it hits the front left guide bar and acquires a stable new motion vector. Once the step motor is started, the plate moves orthogonally toward the mechanical elbow, creating two parallel strike-slip shear zones and a divergent (rift) zone above the VD imposed by the fixed plastic sheet (Figure 2b). During the rotation phase, zones of transtension and transpression are created on the right and left sides of the plate, respectively, and an oblique rift develops at the back (Figure 2c). After the rotation, the plate is constrained by the top guide bars, creating new shear zones on each side (Figure 2d) that are oblique to the originals.

3.3. Model Rheology and Materials Used

Our brittle/ductile models represent a two-layer continental crust, while the brittle-only model represents a single layer of oceanic crust (Figure 3). Layers were as follows:

1. For brittle crust, we use dry feldspar sand (which deforms according to the Mohr-Coulomb criterion) with a density of $\rho = 1.3$ g/cm^3 (Luth et al., 2010), sieved to a grain size $d = 100$–350 μm, and an internal friction coefficient of μ_{fric} of 0.6 (Sokoutis et al., 2005).

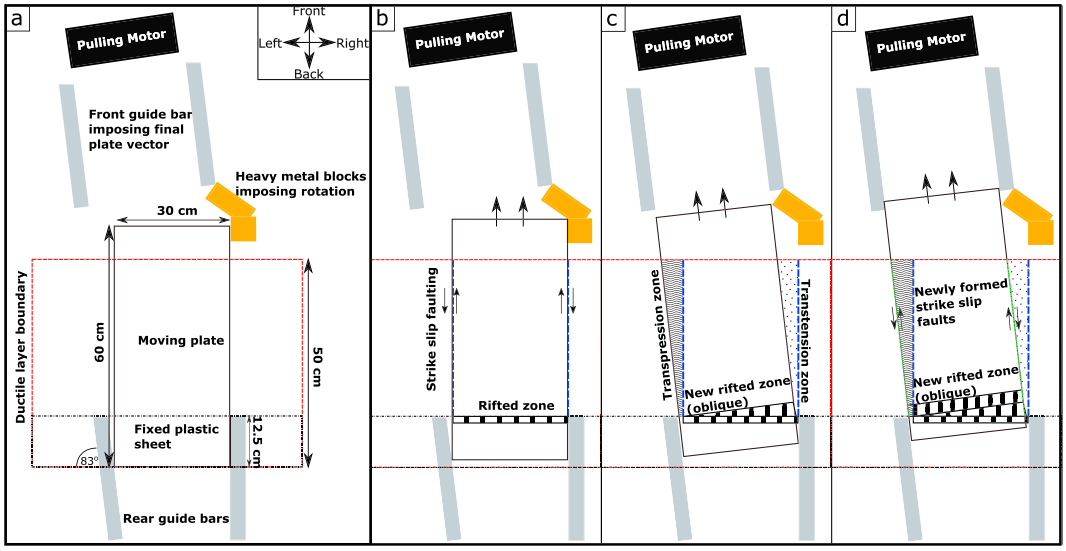

Figure 2. Model array: (a) initial configuration and dimensions, (b) orthogonal motion stage, (c) end of rotation stage, and (d) new oblique plate motion vector stage.

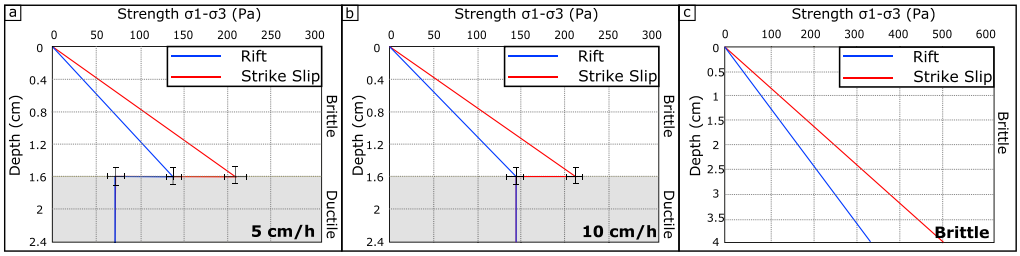

Figure 3. Model strength profiles: (a) 5 cm/hr model run (weak brittle/ductile coupling), (b) 10 cm/hr model run (strong brittle/ductile coupling), and (c) brittle only run (oceanic crust). White background = brittle layers, grey background = ductile layers.

2. Ductile crust is represented by transparent silicone putty SGM-36 in the PDMS group, a polydimethyl siloxane with a density of $\rho = 0.970$ g/cm^3, no yield strength, and viscosity at room temperature of $\mu_{vis} = 5{\times}10^4$ Pa·s (Weijermars, 1986a, 1986b; Weijermars, 1986c).

The governing equations for the strength in each layer are derived from Brun (2002). For the brittle layers, the strength profile along the strike slip fault is given by the equation:

$$\sigma 1{-}\sigma 3_{(ss)} = \rho g h_b \tag{1}$$

where $\sigma 1 - \sigma 3_{(ss)}$ is the brittle layer strength along the fault, g is the gravitational acceleration, and h_b is the thickness of the sand layer.

For extension in the brittle layers, the governing equation is as follows:

$$\sigma 1{-}\sigma 3_{(r)} = \frac{2}{3}(\sigma 1{-}\sigma 3)_{(ss)} \tag{2}$$

where $\sigma 1$ — $\sigma 3_{(r)}$ is the extending brittle layer strength.

For the ductile layer, the strength is as follows:

$$\sigma 1{-}\sigma 3_{(d)} = 2\left(\eta \frac{V}{h_d}\right) \tag{3}$$

where $\sigma 1 - \sigma 3_{(d)}$ is the ductile layer shear strength, η is the ductile layer viscosity, V is the pulling velocity, and h_d is ductile layer thickness.

These equations produce the rheological profiles shown in Figure 3. These strength profiles apply only to the very early stages of deformation in each experiment.

3.4. Scaling

Scaling of our analogue models to their natural prototypes was based on Ramberg's (1981) principles of maintaining similarity in the geometry of the structures, the kinematic evolution of the models, and the rheology of the crust in each model run. In the brittle/ductile models, the 2.4-cm-thick model corresponds to 15 (Persaud et al., 2015) to 25 km (Lizarralde et al., 2007) of upper and lower continental crust in the GoC. This results in a prototype to model ratio $T = T_p/T_m$ of 0.625×10^7 to 1.041×10^7, meaning 1 cm in the experiment equals between 6 and 10 km in nature. In the brittle-only configuration, the 4 cm of model thickness corresponds to about 4–5 km of oceanic crust near the DFZ (Phethean et al., 2016), with a ratio of 1×10^6. To scale the experimental velocity, we use the strain rate ratio between the natural example and the model, γ_p/γ_m, where p = prototype, m = model, $\gamma = V/T_d$, V = velocity, and T_d = ductile layer thickness. The N. GoC has had a relative plate velocity of 30–50 mm/a for at least 12 Ma (Brune et al., 2016), and the thickness of the crust before extension is estimated at 10–15 km in the north to 20–25 km in the South (González-Fernández et al., 2005; Lizarralde et al., 2007). The strain rate ratio is thus $2.2–8.8 \times 10^{-3}$, so 5 cm/hr corresponds to 13–50 mm/a in nature, and 10 cm/hr to 25–100 mm/a.

3.5. Limitations

Our model does not have 100% orthogonal motion in the first centimeter of deformation. However, when scaled to the natural examples, the deviation (approximately 0.5–1°) would still be classified as an orthogonal rift within experimental limits. For the brittle/ductile configuration, the experimental runs are stopped before the ductile layer is ruptured completely. In nature, that would translate to the moment before continental rupture. Thus, strictly speaking, the structures created are not transform faults but strike-slip faults or shear zones that would then be classified as transform faults after the onset of rupture. However, the transpressional and transtensional structures would remain imprinted on the margins, indicating past plate motion changes. Since our models represent only the crust, we are obliged to assume that the mantle underneath accommodates this motion. As in most brittle/ductile analogue models, there is no isostatic compensation, which contributes to the differences between the natural examples and our models (Schellart & Strak, 2016). Finally, we do not account for the effects of erosion or heat transfer between the layers.

4. Results

We describe the fault kinematic evolution in the experiments, based on observations from top-view time-lapse images (Figures 4, 5, and 6) and cross sections from the end of each model run. We use the topography derived from the surface scanning in order to identify normal/reverse motion in faults and the pink marker lines in the top-view time-lapse images to identify strike-slip motion and temporal relationships between faults.

4.1. Experiment 1 (Weak Brittle-Ductile Coupling)

4.1.1. Orthogonal Stage

Transtension Side: After ~1.8 cm of orthogonal motion, a series of dextral Riedel (R) faults develops from the trailing edge of the plate, propagating toward the rift (Figure 4e). A series of higher-angle shear structures develops near the front of the moving plate boundary, potentially representing P shears (Tchalenko, 1970). The development of en-echelon strike-slip faults in this broad zone forms the initial transtensional shear margin. This zone is wider further away from the rift, with a maximum width of ~4 cm. Closer to the rift, there is no visible surface rupture, but localization of this motion on incipient faults can be seen from the displacement of the pink marker lines.

Transpression Side: At the other boundary, fault formation appears to be incipient throughout, with no surface expression apart from displacement of marker lines (Figures 4f and 4n). However, in the outer part of the plate boundary, a thrust front appears to form. This is due to the freedom of movement of the plate, which has already started rotating to produce the first transpressional features.

Rift: The rift zone in the back is focused on two main faults and has similar width throughout (Figures 4m and 4n).

4.1.2. Rotation Stage

Transtension Side (Start of Rotation): After 2.5 cm of movement, the plate reaches the mechanical elbow, initiating rotation. The P shears described in the orthogonal stage now develop a normal-oblique slip character (Figure 4g). New strike-slip faults also form which cross-cut older structures to accommodate the rotating motion vector. The surface expression of horizontal motion propagates backward in a diffuse zone ~5 cm wide as a series of strike-slip faults. On the fixed part of the experiment, the outermost faults in the transtension zone start to develop a normal-oblique slip character, as they no longer accommodate exclusively horizontal motion, and distinct fault scarps begin to form along them (Figure 4g). The topography change (Figure 4o) indicates that the biggest depression lies at the front end of the moving plate, further from the pole of rotation, where plate separation is much larger.

Transpression Side (Start of Rotation): Here horizontal motion is accommodated by one main fault, which displays an oblique-reverse component (Figure 4h). Similar to the transtension side, the locus of deformation is focused near the front end of the moving plate, where plate overlap is significantly greater, resulting in a higher degree of compression (Figure 4p).

Transtension Side (End of Rotation): After approximately another 2.5 cm of movement (5 cm total), displacement takes place along a narrow zone of strike-slip faulting, the principal displacement zone (PDZ; Figure 4i). The PDZ now extends back to the rift-transform intersection (RTI) and is encased on both

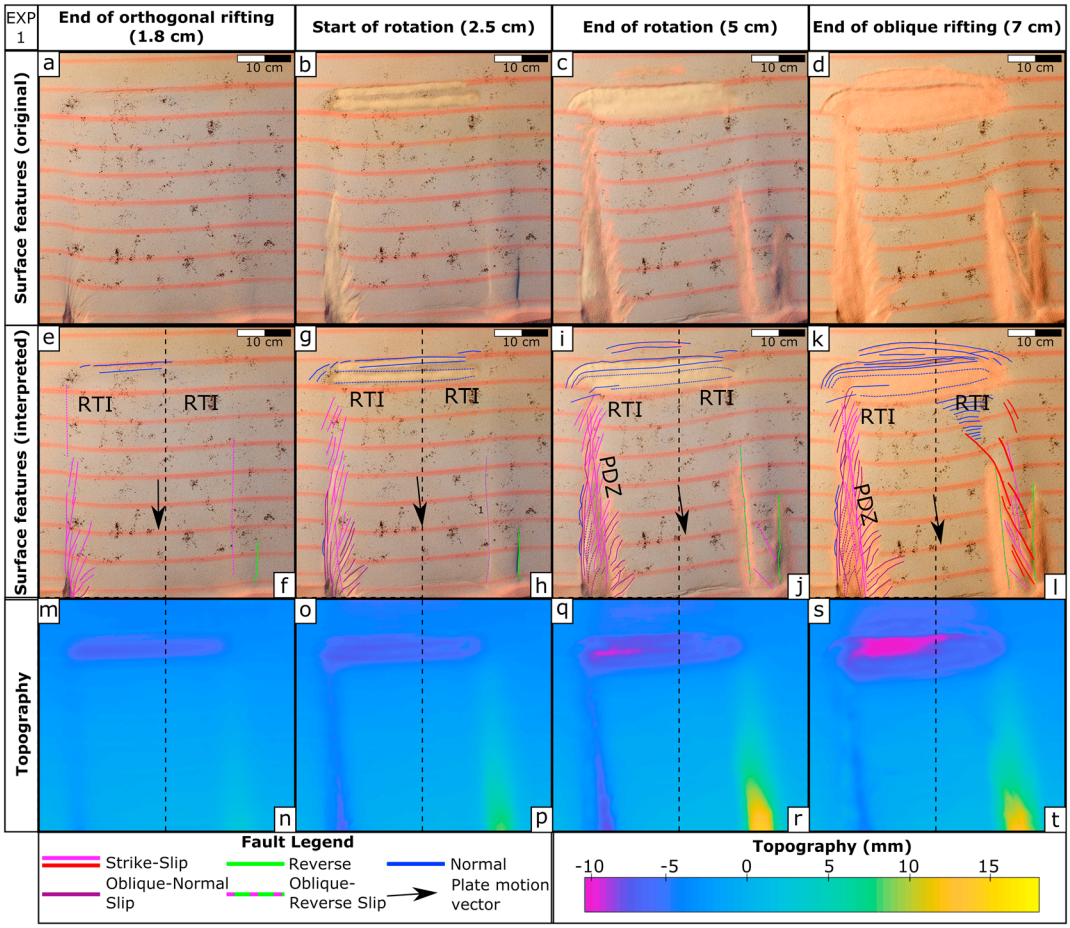

Figure 4. Experiment 1 (5 cm/hr). (a–d) Surface feature development. (e–l) Surface feature development (interpreted). (m–t) Topography development. Figure split into transtensional (e, g, i, k, m, o, q, s) and transpressional side (panels f, h, j, l, n, p, r, t). PDZ = principal displacement zone, RTI = rift-transform intersection. Note the evolution of normal faulting (blue faults) in the top of (e)–(l). In the midsection of each panel, note the evolution of transtensional (pink/purple faults) and transpressional (pink/green faults) deformation zones. The red faults in panel l correspond to the last strike-slip faults formed in the experiment. For higher-resolution uninterpreted top views, see Figures S1–S4.

sides by oblique-normal faulting (Figure 4i). The topography shows further deepening occurring here (Figure 4q).

Transpression Side (End of Rotation): At the end of the 7° plate rotation, the horizontal and vertical motions are still accommodated by the same two faults created at the start of the rotation phase (Figure 4j). Between those two faults, the total model thickness has increased by around 45% (Figure 4r).

Rift: The rift starts to develop an oblique character during the rotation, with the initiation of curved faults on its flanks (mainly on the transtensional side; Figures 4g and 4i). By the end, it is already asymmetrical, ~4 cm wide at the transpressional RTI and ~6 cm at the transtensional RTI (Figures 4o–4r). Further extension in the rift zone now propagates behind the initial rift zone (closer to the fixed plastic sheet) through a new graben (Figure 4i).

4.1.3. Final Plate Vector Stage

Transtension Side: The plate now has its final plate motion vector. After 2 cm of motion (7 cm in total), the PDZ is clearly more developed, with strike-slip faults extending all along the edge of the moving plate (Figure 4k). The majority of the P shears (with the exception of those adjacent to the RTI) are now oblique-normal, shown by the presence of fault scarps (Figures 4k and 4s).

Transpression Side: The zone of transpression is now cross-cut by a series of strike-slip faults with clear-surface expressions that accommodate horizontal motion between the two main thrust fronts (Figure 4l).

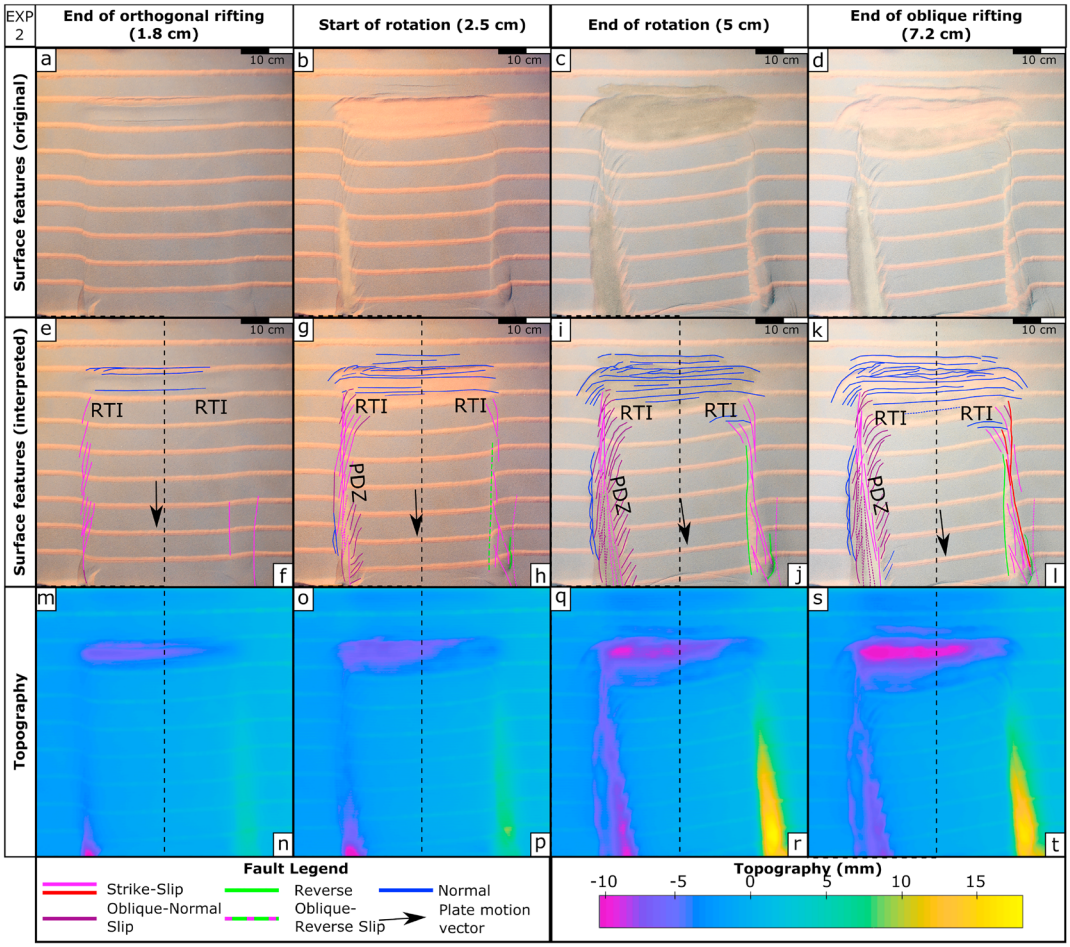

Figure 5. Experiment 2 (10 cm/hr). (a–d) Surface feature development. (e–l) Surface feature development (interpreted). (m–t) Topography development. Panels and abbreviations as in Figure 4. Note the evolution of normal faulting (blue faults) in the top of (e)–(l). In the midsection of each panel, note the evolution of transtensional (pink/purple faults) and transpressional (pink/green faults) deformation zones. The red faults in panel l correspond to the last strike-slip faults formed in the experiment. For higher-resolution uninterpreted top views, see Figures S5–S8.

Furthermore, at the inside corner of the RTI, a triangular-shaped series of normal faults has developed, bounded by a strike-slip fault. Reverse faulting appears to have stopped, and the motion is now purely horizontal with the original uplifted zone cross-cut by the newly formed strike-slip faults (Figure 4t).

Rifting: The new oblique rift is now very asymmetrical, with the part near the transtensional RTI >10 cm wide, while the part in the transpressional RTI is ~7 cm (Figures 4s and 4t). Topography (Figure 4s) shows the locus of deformation focused in a 1-cm-deep depression near the transtensional RTI. New faults have formed at the back of the rift zone in the newly added sediments to accommodate the continuing extension. These faults appear to be oriented orthogonally to the new extension direction vector. The arcuate faults in the back now extend the whole length of the rift (Figures 4k and 4l).

4.2. Experiment 2 (Strong Brittle-Ductile Coupling)

4.2.1. Orthogonal Stage

Transtension Side: After ~1.8 cm of orthogonal motion, a series of dextral Riedel (R) faults develops from the edge of the moving plate, propagating toward the trailing edge of the plate (Figure 5e). The first structure in the bottom of the panel is boundary related and thus is not interpreted as an R fault. The initial transtensional shear zone is ~4 cm wide throughout.

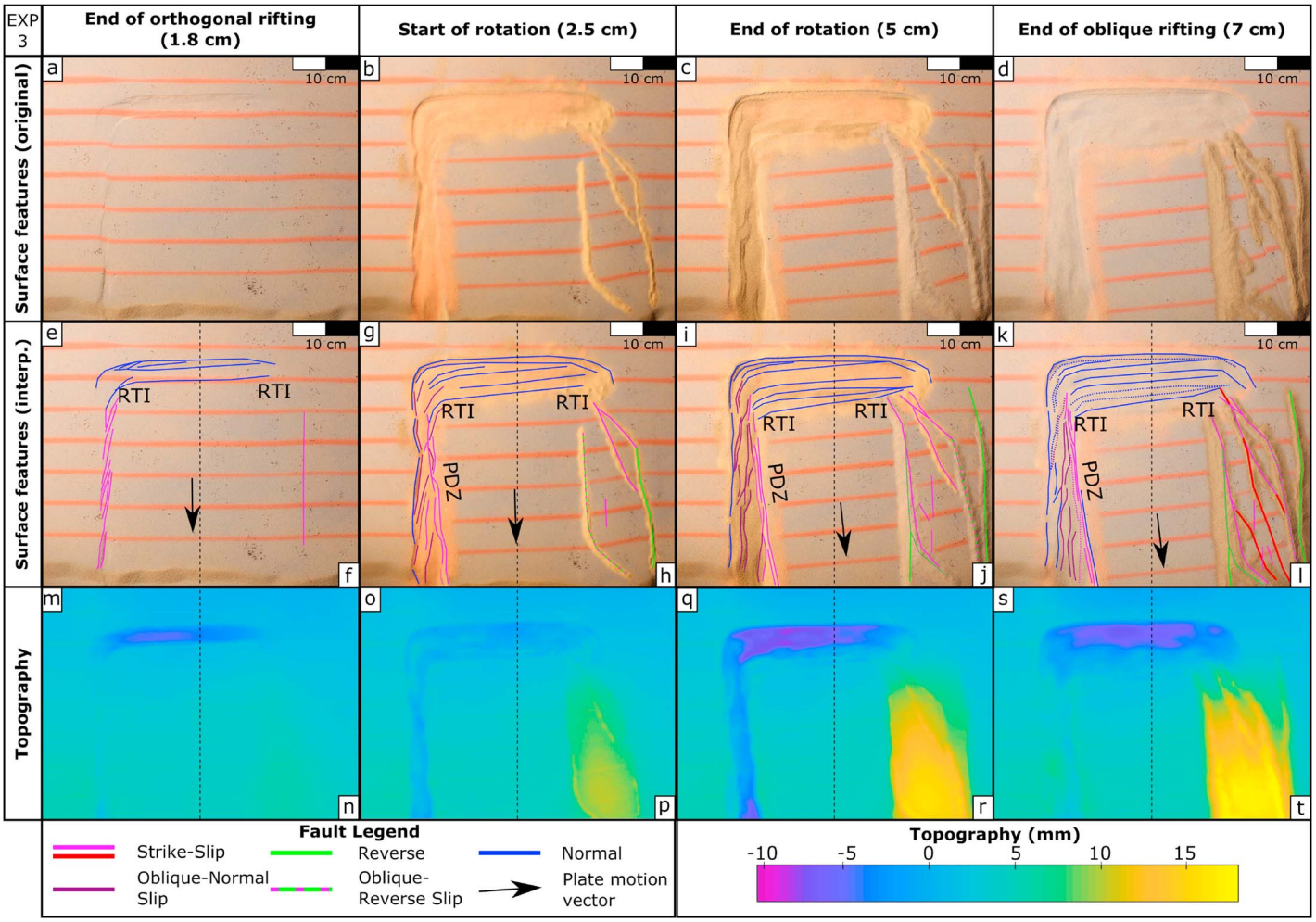

Figure 6. Experiment 3 (brittle only). (a–d) Surface feature development. (e–l) Surface feature development (interpreted). (m–t) Topography development. Panels and abbreviations as in Figure 4. Note the evolution of normal faulting (blue faults) in the top of (e)–(l). In the midsection of each panel, note the evolution of transtensional (pink/purple faults) and transpressional (pink/green faults) deformation zones. The red faults in panel l correspond to the last strike-slip faults formed in the experiment. For higher-resolution uninterpreted top views, see Figures S9–S12.

Transpression Side: Any strike-slip faulting appears to be incipient and is only observable in the displacement of the pink marker lines (Figure 5f). However, the topography shows a slight rise of 3–5 mm, indicating the initiation of transpression in the area due to free plate movement (Figure 5n).

Rift: Rifting over the VD is considerably wider this time and is focused in three main fault zones. The width of the rift is ~5 cm with curved faults developing at the edges (Figures 5e, 5f, 5m, and 5n).

4.2.2. Rotation Stage

Transtension Side (Start of Rotation): After 2.5 cm of approximately orthogonal movement, the plate reaches the mechanical elbow, initiating rotation. A series of higher-angle shear structures has developed, potentially representing P shears (Figure 5g). These are oblique-normal, as there are clearly visible fault scarps along them (Figure 5o). A few are more pronounced toward the RTI, displaying a horsetail splay character (Figure 5g). A PDZ develops at this stage, comprising a series of strike-slip faults aligned from the front to the trailing end of the moving plate, accommodating horizontal motion. Figure 5o shows that the deepest depression is located at the front end of the moving plate.

Transpression Side (Start of Rotation): Here horizontal motion is accommodated by an oblique-reverse fault and a series of cross-cutting strike-slip faults that are parallel to subparallel to the plate motion vector (Figure 5h). From the cross-cutting relationships between these strike-slip faults, it can be inferred that

those parallel to the current plate vector are the youngest. Furthermore, a series of horsetail splays starts to develop adjacent to the RTI corner (Figure 5h).

Transtension Side (End of Rotation): After approximately another 2.5 cm of plate movement, the PDZ has followed the moving plate's vector change through the development of new motion-parallel en-echelon strike-slip faults, at a 7° orientation to the original (Figure 5i). The PDZ is now fully connected to the RTI at the trailing end of the moving plate. The P shears now extend throughout the right flank of the PDZ and display oblique-normal slip characteristics, with scarps visible in the topography and horizontal motion visible in the overhead views (Figures 5q and 5i). On the fixed side of the experiment, a series of normal faults develops to accommodate the extensional component of the transtensional shear (Figures 5i and 5q). The total width of the transtensional shear zone is ~8 cm throughout, but the PDZ is much narrower (~2.5 cm).

Transpression Side (End of Rotation): At the end of the rotation, the transpression zone has been uplifted more than 15 mm, increasing in thickness by about 60% (Figure 5r). More strike-slip faults have developed, with the newest formed parallel to the new plate motion vector, as inferred from their cross-cutting relationships (Figure 5j). Furthermore, near the RTI corner, the horsetail splays have developed further and are now accompanied by two normal faults. Finally, the initial oblique-reverse faults now only accommodate thrusting motion, as interpreted from the overhead views.

Rift: The rift acquires an oblique character during the rotation stage. A series of arcuate faults develops on its sides (mainly on the transtensional side; Figures 5g and 5i). By the end of plate rotation, it is clearly asymmetrical, ~7 cm wide at the transpressional RTI and ~12.5 cm wide at the transtensional RTI (Figures 5q and 5r). Further extension in the rift zone propagates at the back of the initial rift zone (closer to the fixed plastic sheet) through a series of new grabens (Figures 5i and 5j).

4.2.3. Final Plate Vector Stage

Transtension Side: The plate now has acquired its final directional vector. After another 2.7 cm of motion (7.2 cm in total), the PDZ has developed further. The horsetail splays in the RTI are more pronounced and merge with the rift faults, giving the RTI a distinct corner shape (Figure 5k). Topographically, the part of the transtensional shear zone closer to the RTI does not appear to have experienced any significant extension apart from the topography disruptions directly above the faults (Figure 5s).

Transpression Side: In the zone of transpressional shear, a series of new motion-parallel faults has developed, similar to those that developed at the end of the rotation stage (Figure 5l). The two long strike-slip faults between the thrust fronts appear to have accommodated all of the horizontal motion. Furthermore, an extensional triangle has developed in the RTI, bounded by a series of horsetail splays. These horsetail splays display an oblique-normal slip character, as is evident from the topographic depression along them (Figure 5t).

Rifting: The new oblique rift is now very asymmetrical, with the part near the transtensional RTI >13 cm wide, while the part in the transpressional RTI is ~7–8 cm (Figures 5s and 5t). Extension is focused in an elongated trough near the transtensional RTI (Figure 5s). Continuing extension is accommodated by newer faults forming at the back of the rift zone. These faults appear to be orthogonal to the original orthogonal plate vector but curve at the ends (Figures 5k and 5l).

4.3. Experiment 3 (Brittle Only)

4.3.1. Orthogonal Stage

Transtension Side: After ~1.8 cm of orthogonal motion, a series of dextral Riedel faults has developed from the edge of the moving plate to the RTI (Figure 6e). These Riedel faults define a series of en-echelon pull-aparts whose depressions can be seen in Figure 6i. The initial transtensional shear zone has a constant width of ~3 cm (Figure 6e).

Transpression Side: Any faulting motion appears to be incipient and only observable in the displacement of the pink marker lines (Figure 6f). However, the topography shows a slight elevation increase of 1–2 mm in a broad triangular zone, indicating the very early stages of transpression due to free plate movement (Figure 6n).

Rift: Rifting initiates over the VD within a relatively narrow, symmetrical zone of extension. Two curved main faults are visible in the transpressional RTI side (Figures 6e and 6f).

4.3.2. Rotation Stage

Transtension Side (Start of Rotation): The moving plate intercepts the mechanical elbow after 2.5 cm of orthogonal movement. The en-echelon pull-apart basins now become more pronounced and start to merge, visible as undulations in topography (Figure 6o). The boundary of the pull-apart basins on the moving plate side is defined by a series of connecting strike-slip faults, representing the PDZ. The extensional component of this transtensional zone is accommodated by a series of oblique-normal and normal faults, representing the other boundary of the pull-apart basins (Figures 6g and 6o).

Transpression Side (Start of Rotation): Two main thrust fronts develop over the overlapping plate boundary (Figure 6p). The fault situated above the moving plate displays an oblique-reverse slip character (Figure 6h). Between these two reverse faults, a series of strike-slip faults starts to develop, forming the initial RTI.

Transtension Side (End of Rotation): After approximately another 2.5 cm of plate movement, the PDZ has rotated a total of 7°, following the moving plate's vector change through the development of new motion-parallel strike-slip faults (Figure 6i). The PDZ is now fully connected to the RTI, forming a corner shape. The pull-apart basins have now almost completely merged, with similar depth across them (Figure 6q). The oblique-normal faults in the flanks of the fixed side of the experiment have also developed further (Figures 6i and 6q).

Transpression side (End of Rotation): By the end of the rotation, new strike-slip faults have developed parallel to the new plate vector. The second of the two original thrust fronts (Figure 6h) has now also acquired an oblique component, as indicated by the displacement of the pink marker lines (Figure 6j). Topographically, the area has been thickened by ~25% between the two main thrust fronts (Figure 6r). Finally, another thrust front has formed at the right side of the transtensional shear zone (Figure 6j), potentially a boundary effect.

Rift: The rift acquires an oblique character in the rotation stage, with a series of arcuate faults developing on both sides (Figures 6g, 6h, 6i, and 6j). The obliquity leads to the rift being ~7 cm wide at the transpressional RTI and ~11 cm wide at the transtensional RTI (Figures 6i and 6j).

4.3.3. Final Plate Vector Stage

Transtension Side: The plate now has acquired its final directional vector, and we observe only horizontal motion. After 2 cm of further motion (7 cm in total), the PDZ is in the same location, following the motion of the moving plate (Figure 6k).

Transpression Side (End): The new motion has now produced three long subparallel strike-slip faults that cross-cut the preexisting ones (Figure 6l). These faults extend from the front end of the moving plate to the RTI.

Rifting: The oblique rift is now more asymmetrical, >12 cm wide near the transtensional RTI and ~8 cm in the transpressional RTI (Figures 6k, 6l, 6s, and 6t).

5. Discussion

5.1. Comparison With Natural Examples

5.1.1. Gulf of California

We use the high-resolution UL9905 seismic data set (Stock et al., 2015) to compare profiles in the northern GoC with profiles through the transtensional side of Experiment 2 (Figure 7). The N. GoC is thought to have undergone a plate rearrangement around 3 Ma, which corresponds to Unit 8 (yellow in Figures 7c and 7f; Martín-Barajas et al., 2013). The seismic data set images the first few kilometers of the crust, but it is reasonable to assume that the structures extend deeper and thus would scale to our models. The early stages of evolution of the transtensional side of Experiment 3 (Figures 6e, 6g, and 6i) are also compared with the evolution of the whole GoC area from 12.5 Ma onward (Figures 1d, 1e, and 1f).

The fault patterns overall appear similar. In the northern GoC, there is a series of sigmoidal normal faults at the NW edge of the Ballenas Transfrom Fault Zone (Figure 7a), similar to the series of horsetail splays formed at the end of Experiment 2, which appear to almost merge with the rift (Figure 7b). These sigmoidal faults accommodate the discrepancy between the plate motion vector and the direction of extension.

10.1029/2018TC005261

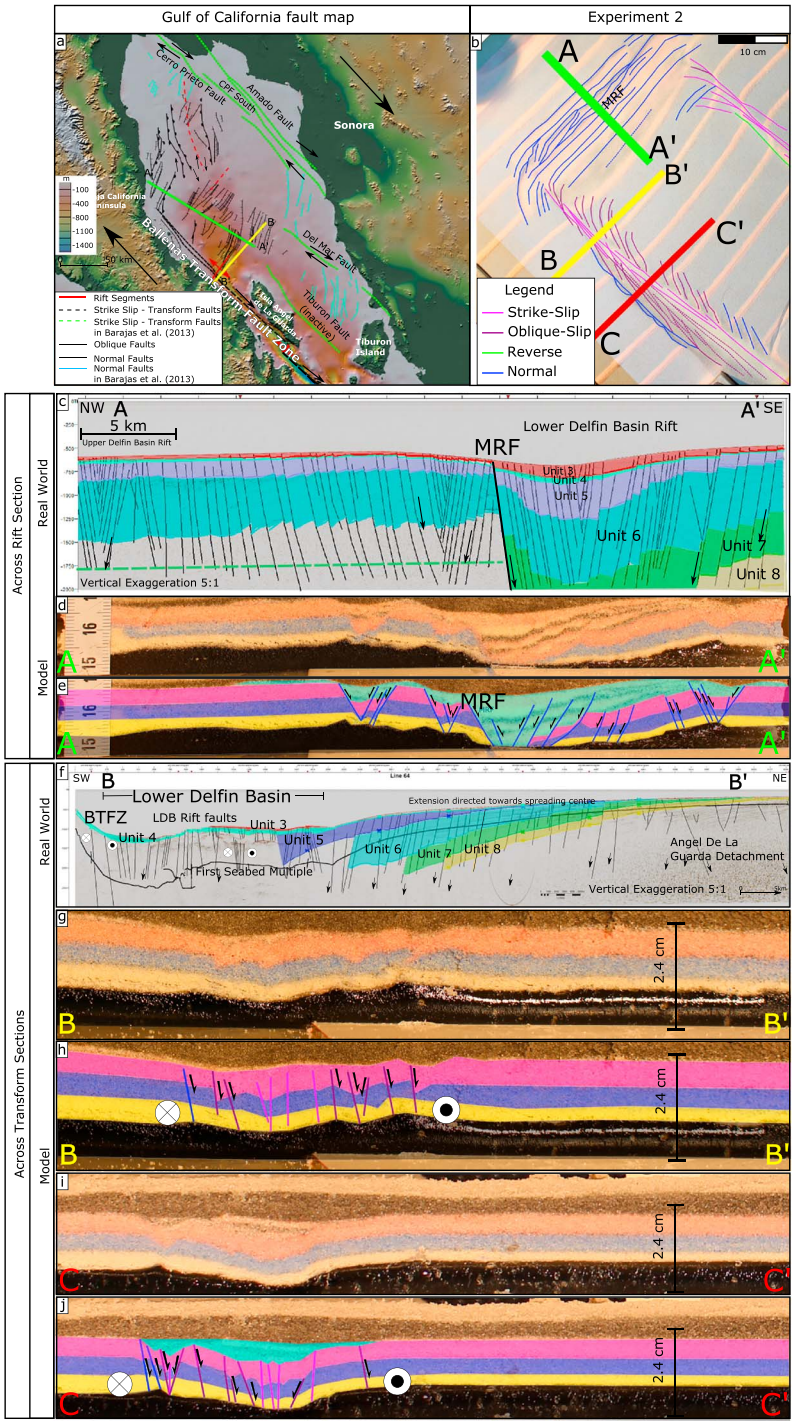

Figure 7. Comparison between Experiment 2 and seismic cross sections from the N. Gulf of California (GoC). (a) Surface fault patterns in the N. GoC (modified after Persaud et al., 2003, and Martín-Barajas et al., 2013). (b) Surface fault patterns in Experiment 2. (c, d, e) Comparison between a seismic cross section across the Lower Delfin Basin spreading center and a section across the rift of Experiment 2. MRF = main rift fault. (f, g, h, i, j) Comparison between a seismic cross section across the Ballenas Transform Fault Zone (BTFZ) and two sections across the transtensional rift-transform intersection of Experiment 2. Original model layering from bottom to top: black, yellow, blue, pink. In (e) and (j), the blue-shaded alternating white, black, and pale pink top layers represent the sediments added during the model run. The brown and white/cream layers above the models are the protective layer added before cutting. Seismic interpretations from the UL9905 high-resolution reflection seismic data set (Stock et al., 2015). Bathymetry from GMRT grid version 3.3. For higher-resolution uninterpreted model sections, see Figures S13–S15.

We next compare the change in fault motion and development due to the change in plate motion. In our model, faults that were strike-slip during the initial orthogonal phase (Figure 5g) became either oblique-normal or purely normal by the end of the rotation. Horizontal motion became concentrated on faults aligned with the new plate vector (Figures 5i and 5k). This is analogous to examples of large transform faults in the northern GoC. These faults, such as the Tiburon fault, accommodated plate motion before the change in extension direction (Figure 7a). They were then abandoned because of this rotation and became either oblique-normal or purely extensional structures.

Figures 7f, 7g, 7h, 7i, and 7j compare two sections across the dextral transform adjacent to the RTI in Experiment 2 with a seismic cross section across the dextral Ballenas Transform Fault Zone. The strike-slip motion is accommodated by a main transtensional shear zone. Deformation is partitioned, with horizontal motion taken up by strike-slip and oblique-normal faults (Figures 7f, 7g, 7h, 7i, and 7j). The latter also accommodate the extensional component of the tectonic regime, producing a topographic depression. This extension shifts northward with time, reflected in the northward migration of the locus of sedimentation. A similar pattern is observed in the syn-rift layers of our models (Figures 7g, 7h, 7i, and 7j). In the northern GoC, a series of oblique-normal faults on the Baja California peninsula also accommodates that oblique motion (Bennett & Oskin, 2014).

We then compare a seismic profile across the Lower Delfin Basin rift (Figure 7c) with a profile across the rift in Experiment 2 (Figures 7d and 7e). In both, rifting is controlled by one major rift fault (MRF), accompanied by a series of antithetic faults on the opposite side (Figures 7c, 7d, and 7e). A series of smaller grabens has also developed in the back of each rift. This is located directly NW of the MRF in Figure 7c for the northern GoC and to the left of the MRF in Figures 7d and 7e. The syn-sedimentary sequence is thickest over the main part of the rift. This is represented by the blue-shaded alternating white, black, and pale pink units above the pink layer in the model (Figures 7d and 7e) and the yellow layer Unit 8/Top Pliocene in the seismic cross section (Figure 7c; Martín-Barajas et al., 2013).

Finally, we compare the evolution of the whole GoC since 12.5 Ma with the surface evolution of the transtensional side of Experiment 3. We see a direct correlation in how the transtensional boundary evolves when a change in extension direction is imposed. In the beginning, Bennett et al. (2013) argue that shearing was localized in en-echelon dextral strike-slip shear zones (Figures 1d and 6e). These shear zones evolved into pull-apart basins that formed the proto-Gulf (Figures 1e and 6g). Finally, when the extension direction changes, the margins of the GoC began to drift apart at varying rates (Figures 1f and 6i).

5.1.2. Tanzania Coastal Basin

The TCB underwent a plate reorganization ~150 Ma, resulting in the formation of the DFZ. In both Experiment 3 (Figure 8b) and the TCB (Figures 1g–1l and 8a), zones of compression develop adjacent to the main strike-slip structures as the motion changes, and the pattern of strike-slip faults evolves to accommodate the changed angle. In Experiment 3, some of the initial strike-slip faults are abandoned after the change in motion (Figures 6j, 6l, 8a, and 8b—pink faults). Those that remain active reorient themselves by developing kinks, leading to a curved surface expression that is not completely aligned with the final plate motion (Figures 6l, 8a, and 8b—red faults). The DFZ shows a similar pattern: the earliest transform faults have been abandoned, and the DFZ has a slightly kinked, 'open S' shape, reflecting this two-stage history (Figure 8a; Phethean et al., 2016).

The deep seismic cross section from the DFZ (Figure 8c) shows clear evidence for intraplate compressional deformation. The same coexistence of strike-slip and compression is apparent in the two profiles across the transpressional side of Experiment 3 (Figures 8d, 8e, 8f, and 8g). During the plate rotation in Experiment 3, the compressional structures form to accommodate that component of motion (Figures 6h and 6j). These structures stop developing after rotation has ceased, when only the large strike-slip faults are active (Figure 6l). We can thus infer that intraoceanic crustal thrusting may have occurred in the TCB to accommodate the plate motion change around 150 Ma, prior to the complete development of the DFZ. This is further supported by Sauter et al. (2018), who date the uppermost syn-deformational sediments (Figure 8c) as pre-Aptian (125 Ma). In the model cross sections (Figures 8d, 8e, 8f, and 8g), thrusts develop on both sides of the strike slip zone, but this is not observed in the seismic example (Figure 8c). This is because the crust to the east of the DFZ is much younger and formed as the MOR passed this location, marking the end of deformation in this region. During the Jurassic, there probably was deformed crust on

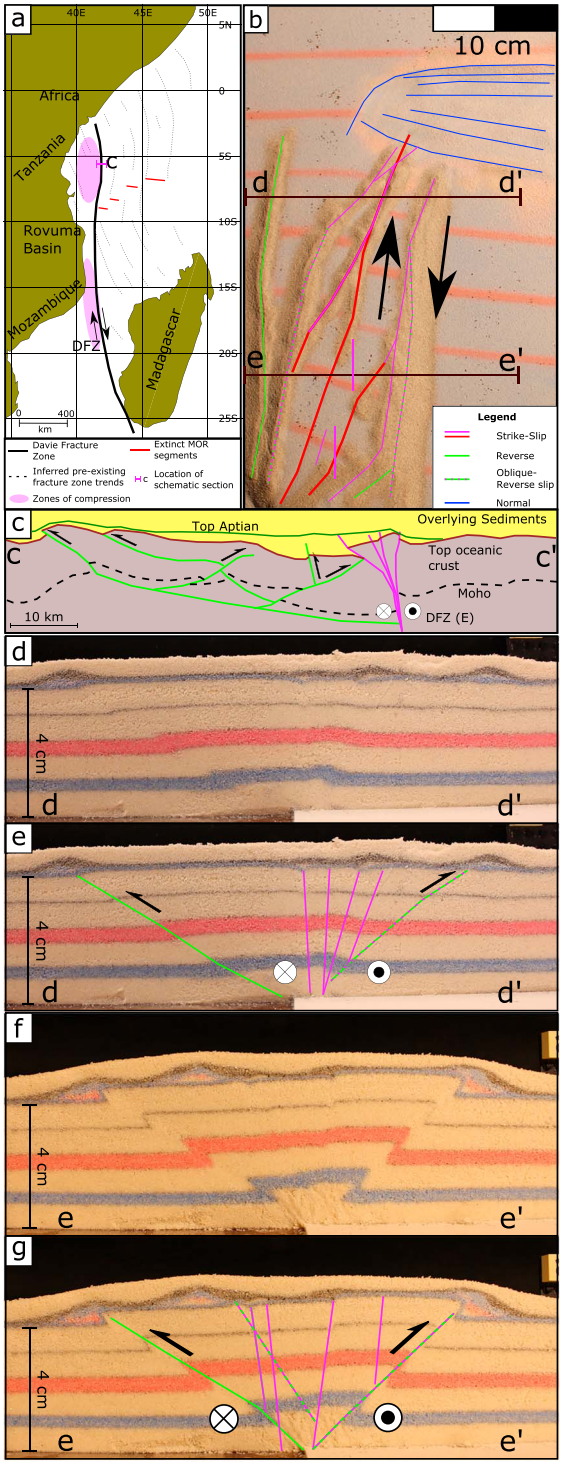

Figure 8. Comparison between the Tanzania Coastal Basin (TCB) and Experiment 3. (a, b) Surface fault patterns in the TCB and Experiment 3, respectively. (c) Schematic cross section across the Davie Fracture Zone (DFZ). (d, e, f, g) Cross sections across the transpressional zone of Experiment 3. TCB configuration modified from Phethean et al. (2016). Seismic interpretation in (c) is reinterpreted from Sauter et al. (2018). In (b), the red faults correspond to the last strike-slip faults formed. Syn-tectonic sedimentation above the main structures is a protective layer. For higher-resolution uninterpreted experiment sections, see Figures S16–S17.

both sides of the DFZ here, but the eastern side moved southward with Madagascar and is now likely located in the Morondava Basin.

5.2. Further Discussion

Our results provide good first-order agreement with natural transform plate boundaries that have experienced a change in relative motion during their evolution, resulting in either transpression (TCB) or transtension (GoC). During the initial orthogonal phase, the structures that develop are similar to those observed by Basile and Brun (1999). Faster plate velocity results in strong brittle/ductile layer coupling and diffuse rifting (13 cm at its maximum width; Figure 5s), while slower rifting velocity results in weak brittle/ductile coupling and narrower rifting (10 cm at its maximum width; Figure 4s). Other parameters that can affect the model rheology and thus the rift width, such as the thickness of the brittle layer (Vendeville et al., 1987), are held constant, so the difference is due to the strain contrast between the layers being minimized when a higher velocity is imposed (Brun, 2002). The same appears to be the case even when rifting is oblique.

The opposite appears to be the case in the transtensional and transpressional shear zones. The transtensional shear zone in Experiment 1 reaches widths between 5 and 10 cm (Figure 4s), while in Experiment 2 it has a constant width of about 5–6 cm throughout (Figure 5s). Similarly, the transpressional zone of Experiment 2 (Figure 5t) is 50% narrower than the one in Experiment 1 (Figure 4t). This corresponds to natural transform examples where faster transforms have narrower deformation zones (see Table 1 of Mauduit & Dauteuil, 1996, for spreading velocities and corresponding transform widths). However, all three experiments produce wide zones of oblique lateral deformation, recording several stages of fault evolution. This is consistent with the numerical modeling of Le Pourhiet et al. (2017), who argue that transforms experiencing obliquity do not develop as line segments but form diffuse zones ~100 km wide recording several phases of deformation prior to oblique breakup.

The brittle-only experiment shows good correlation with the evolution of the DFZ. It supports the suggestion by Phethean et al. (2016) that at ~150 Ma a change occurred in the plate motion that was accommodated by compression, with previous transforms cross-cut by a much larger structure that became the DFZ. In our experiment, the initial strike-slip faults become inactive once the final motion vector is established (Figures 6h, 6j, and 6l—pink strike-slip faults). Then, horizontal motion is taken up by new cross-cutting faults parallel to the final plate vector (Figures 6h, 6j, and 6l—red strike-slip faults).

Although the DFZ formed in oceanic crust, there is a strong similarity with the surface features developing on the transpressional part of Experiment 2 (Figure 5l). In particular, a large sigmoidal fault develops in Experiment 2, similar in shape to the DFZ (long red fault in Figure 5l). This could be explained by the strength profile of Experiment 2 (Figure 2b), where the maximum strength of the brittle layer and the ductile layer are almost identical, similar to oceanic lithosphere. Although the model is not scaled to represent oceanic lithosphere, this might potentially explain the morphological similarity.

Another natural example comparable to Experiment 2 is the Gulf of Aden. The Alula-Fartac Transform Fault is not characterized by a single narrow

transform valley but rather by two subparallel 180 × 10-km troughs that join two offset ridge segments (D'Acremont et al., 2010). The spreading direction has recently rotated counterclockwise, resulting in extension in the transform basins (D'Acremont et al., 2010). This results in the transform zones migrating in time and space, similar to Experiment 2.

In the transpressional sides of Experiments 1 and 2, we see a thickness increase in the models of approximately 45% and 60%, respectively (Figures 4t and 5t). Based on our experimental scaling, the crustal thickness range for these experiments is 15–25 km. Such a thickness increase would then imply real-world elevation changes of ~7–11 km for Experiment 1 and 9–15 km for Experiment 2. However, because our scaling is based on the density contrast between the brittle and ductile layers, we need to apply a topographic correction factor C_{Topo} (Schellart & Strak, 2016):

$$C_{\mathrm{Topo}} = \frac{\rho^{m}_{\mathrm{LC}}\left(\rho^{p}_{\mathrm{LC}} - \rho^{p}_{\mathrm{UC}}\right)}{\rho^{p}_{\mathrm{LC}}\left(\rho^{m}_{\mathrm{LC}} - \rho^{m}_{\mathrm{UC}}\right)} \tag{4}$$

where ρ^{m}_{LC} is the model's lower crust density (0.970 g/cm^3), ρ^{p}_{LC} is the natural example's lower crustal density (2.9 g/cm^3), ρ^{m}_{UC} is the model's upper crustal density (1.3 g/cm^3), and ρ^{p}_{UC} is the natural example's upper crustal density (2.7 g/cm^3).

Applying equation (4) to our experiments, C_{Topo} is ~0.209, which would reduce the thickness changes to physically reasonable values of 1.4–2.3 km for Experiment 1 and 1.9–3.1 km for Experiment 2. In addition, the analogue models do not include isostatic compensation, which would further reduce the amount of crustal thickening expressed as topographic relief, perhaps by up to a factor of 2 (Schellart & Strak, 2016). Erosion would also reduce the topography.

Nonetheless, our experiments show that overlapping, transpressional transform margins are accompanied by topographic highs parallel to the plate motion. Features such as marginal ridges or plateaus (Mercier de Lépinay et al., 2016) are observed at transform margins that have experienced overlapping plate motions such as the Exmouth Plateau (Whittaker et al., 2016), the Romanche Fracture Zone (Davison et al., 2016), and, in our example, the Davie Ridge. As Euler poles typically migrate over a few million years, other examples of these transpressive or transtensional feature might be preserved where oceanic fracture zones change curvature, indicating a past change in spreading direction (e.g., Iaffaldano et al., 2012; Schettino, 2015).

6. Conclusions

A series of experiments designed to simulate the effects of a change in plate motion on transform margins and RTIs produces structural patterns and topographic effects that show good agreement with natural examples. They provide an understanding of the fault geometries and kinematics and the temporal and spatial relationship of structural features that develop in transtensional and transpressional margins. These are caused by underlap or overlap on the transform margin when the plate motion vector changes.

In transtensional margins, such as the Gulf of California or the Gulf of Aden, we find oblique-normal faults that have developed from original strike-slip faults. These oblique-normal faults accommodate the extensional component of the plate rotation. As the plate vector changes, the PDZ's direction also rotates to accommodate the new horizontal motion.

In transpressional margins, such as the TCB, we report thrust fronts developing to accommodate plate overlap. These thrust fronts are also often oblique and are accompanied by strike-slip faults. As motion in the new direction continues, newer strike-slip faults develop and cut through the preexisting fabric. This is observed both in our lab experiments and in the natural example of the DFZ.

Acknowledgments
The unprocessed data supporting the analysis and conclusions are available online through the open access repository: (http://doi.org/10.5281/zenodo.1321232). The work contained in this paper contains work conducted during a PhD study undertaken as part of the Natural Environment Research Council (NERC) Centre for Doctoral Training (CDT) in Oil and Gas (grant NEM00578X/1). It is cosponsored by Durham University whose support is gratefully acknowledged. L. M. K. is supported by a Royal Society of Edinburgh Personal Research Fellowship funded by the Scottish Government. We thank Antoine Auzemerry for assisting with the experimental set-up and the laser scanning operation and the Editor L. Jolivet, the Associate Editor, A. Schettino, and two anonymous reviewers for their helpful comments.

References

Acocella, V., Faccenna, C., Funiciello, R., & Rossetti, F. (1999). Sand-box modelling of basement-controlled transfer zones in extensional domains. *Terra Nova*, *11*(4), 149–156. https://doi.org/10.1046/j.1365-3121.1999.00238.x

Allemand, P., & Brun, J. (1991). Width of continental rifts and rheological layering of the lithosphere. *Tectonophysics*, *188*(1–2), 63–69. https://doi.org/10.1016/0040-1951(91)90314-I

Atwater, T., & Stock, J. (1998). Pacific-North America plate tectonics of the Neogene southwestern United States: An update. *International Geology Review*, *40*(5), 375–402. https://doi.org/10.1080/00206819809465216

Autin, J., Bellahsen, N., Leroy, S., Husson, L., Beslier, M., & d'Acremont, E. (2013). The role of structural inheritance in oblique rifting: Insights from analogue models and application to the Gulf of Aden. *Tectonophysics*, *607*, 51–64. https://doi.org/10.1016/j.tecto.2013.05.041

Axen, G. (1995). Extensional segmentation of the main gulf escarpment, Mexico and United States. *Geology*, *23*(6), 515–518. https://doi.org/10.1130/0091-7613(1995)023<0515:ESOTMG>2.3.CO;2

Basile, C. (2015). Transform continental margins—Part 1: Concepts and models. *Tectonophysics*, *661*, 1–10. https://doi.org/10.1016/j.tecto.2015.08.034

Basile, C., & Brun, J. P. (1999). Transtensional faulting patterns ranging from pull-apart basins to transform continental margins: An experimental investigation. *Journal of Structural Geology*, *21*(1), 23–37. https://doi.org/10.1016/S0191-8141(98)00094-7

Bellahsen, N., Leroy, S., Autin, J., Razin, P., d'Acremont, E., Sloan, H., et al. (2013). Pre-existing oblique transfer zones and transfer/transform relationships in continental margins: New insights from the southeastern Gulf of Aden, Socotra Island, Yemen. *Tectonophysics*, *607*, 32–50. https://doi.org/10.1016/j.tecto.2013.07.036

Bennett, S. E. K., & Oskin, M. E. (2014). Oblique rifting ruptures continents: Example from the Gulf of California shear zone. *Geology*, *42*(3), 215–218. https://doi.org/10.1130/G34904.1

Bennett, S. E. K., Oskin, M. E., & Iriondo, A. (2013). Transtensional rifting in the proto-Gulf of California near Bahía Kino, Sonora, México. *GSA Bulletin*, *125*(11–12), 1752–1782. https://doi.org/10.1130/B30676.1

Bennett, S. E. K., Oskin, M. E., Iriondo, A., & Kunk, M. J. (2016). Slip history of the La Cruz fault: Development of a late Miocene transform in response to increased rift obliquity in the northern Gulf of California. *Tectonophysics*, *693*, 409–435. https://doi.org/10.1016/j.tecto.2016.06.013

Bird, D. (2001). Shear margins. *The Leading Edge*, *20*(2), 150–159. https://doi.org/10.1190/1.1438894

Brun, J. (2002). Deformation of the continental lithosphere: Insights from brittle-ductile models. *Geological Society, London, Special Publications*, *200*(1), 355–370. https://doi.org/10.1144/GSL.SP.2001.200.01.20

Brune, S., Williams, S. E., Butterworth, N. P., & Müller, R. D. (2016). Abrupt plate accelerations shape rifted continental margins. *Nature*, *536*(7615), 201–204. https://doi.org/10.1038/nature18319

Burov, E. B. (2011). Rheology and strength of the lithosphere. *Marine and Petroleum Geology*, *28*(8), 1402–1443. https://doi.org/10.1016/j.marpetgeo.2011.05.008

Coffin, M. F., & Rabinowitz, P. D. (1987). Reconstruction of Madagascar and Africa: Evidence from the Davie Fracture Zone and Western Somali Basin. *Journal of Geophysical Research*, *92*(B9), 9385–9406. https://doi.org/10.1029/JB092iB09p09385

D'Acremont, E., Leroy, S., Maia, M., Gente, P., & Autin, J. (2010). Volcanism, jump and propagation on the Sheba ridge, eastern Gulf of Aden: Segmentation evolution and implications for oceanic accretion processes. *Geophysical Journal International*, *180*(2), 535–551. https://doi.org/10.1111/j.1365-246X.2009.04448.x

Dauteuil, O., Bourgeois, O., & Mauduit, T. (2002). Lithosphere strength controls oceanic transform zone structure: Insights from analogue models. *Geophysical Journal International*, *150*(3), 706–714. https://doi.org/10.1046/j.1365-246X.2002.01736.x

Dauteuil, O., & Brun, J. (1993). Oblique rifting in a slow-spreading ridge. *Nature*, *361*(6408), 145–148. https://doi.org/10.1038/361145a0

Davis, J. K., Lawver, L. A., Norton, I. O., & Gahagan, L. M. (2016). New Somali basin magnetic anomalies and a plate model for the early Indian Ocean. *Gondwana Research*, *34*, 12–28. https://doi.org/10.1016/j.gr.2016.02.010

Davison, I., Faull, T., Greenhalgh, J., Beirne, E. O., & Steel, I. (2016). Transpressional structures and hydrocarbon potential along the Romanche Fracture Zone: A review. *Geological Society, London, Special Publications*, *431*(1), 235–248. https://doi.org/10.1144/SP431.2

Dorsey, R. J., & Umhoefer, P. J. (2011). Influence of sediment input and plate-motion obliquity on basin development along an active oblique-divergent plate boundary: Gulf of California and Salton Trough. In C. Busby & A. Azor (Eds.), *Tectonics of Sedimentary Basins* (pp. 209–225). Hoboken, NJ: Wiley.

Dubinin, E. P., Grokholsky, A. L., & Makushkina, A. I. (2018). Physical modeling of the formation conditions of microcontinents and continental marginal plateaus. *Izvestiya Physics of the Solid Earth*, *54*(1), 66–78. https://doi.org/10.1134/S1069351318010056

Geiger, M., Clark, D. N., & Mette, W. (2004). Reappraisal of the timing of the breakup of Gondwana based on sedimentological and seismic evidence from the Morondava basin, Madagascar. *Journal of African Earth Sciences*, *38*(4), 363–381. https://doi.org/10.1016/j.jafrearsci.2004.02.003

Gerya, T. (2012). Origin and models of oceanic transform faults. *Tectonophysics*, *522-523*, 34–54. https://doi.org/10.1016/j.tecto.2011.07.006

González-Escobar, M., Suárez-Vidal, F., Sojo-Amezquita, A., Gallardo-Mata, C., & Martin-Barajas, A. (2014). Consag basin: Northern Gulf of California, evidence of generation of new crust, based on seismic reflection data. *International Geology Review*, *56*(11), 1315–1331. https://doi.org/10.1080/00206814.2014.941023

González-Fernández, A., Dañobeitia, J. J., Delgado-Argote, L., Michaud, F., Córdoba, D., & Bartolomé, R. (2005). Mode of extension and rifting history of Upper Tiburón and Upper Delfín Basins, Northern Gulf of California. *Journal of Geophysical Research*, *110*, B01313. https://doi.org/10.1029/2003JB002941

Grokholskii, A. L., & Dubinin, E. P. (2006). Experimental modeling of structure-forming deformations in rift zones of mid-ocean ridges. *Geotectonics*, *40*(1), 64–80. https://doi.org/10.1134/S0016852106010067

Heine, C., Müller, R. D., & Norvick, M. (2002). Revised tectonic evolution of the northwest shelf of Australia and adjacent abyssal plains. In M. Keep, & S. J. Moss (Eds.), *The sedimentary basins of Western Australia 3: Proceedings of the Petroleum Exploration Society of Australia Symposium* (pp. 955–957, chapter: Poster Abstracts). Perth, WA.

Iaffaldano, G., Bodin, T., & Sambridge, M. (2012). Reconstructing plate-motion changes in the presence of finite-rotations noise. *Nature Communications*, *3*(1), 1048. https://doi.org/10.1038/ncomms2051

Le Pichon, X., & Hayes, D. E. (1971). Marginal offsets, fracture zones, and the early opening of the South Atlantic. *Journal of Geophysical Research*, *76*(26), 6283–6293. https://doi.org/10.1029/JB076i026p06283

Le Pourhiet, L., May, D. A., Huille, L., Watremez, L., & Leroy, S. (2017). A genetic link between transform and hyper-extended margins. *Earth and Planetary Science Letters*, *465*, 184–192. https://doi.org/10.1016/j.epsl.2017.02.043

Leroy, S., Razin, P., Autin, J., Bache, F., d'Acremont, E., Watremez, L., Robinet, J., et al. (2012). From rifting to oceanic spreading in the Gulf of Aden: A synthesis. *Arabian Journal of Geosciences*, *5*(5), 859–901. https://doi.org/10.1007/s12517-011-0475-4

Lizarralde, D., Axen, G. J., Brown, H. E., Fletcher, J. M., González-Fernández, A., Harding, A. J., Holbrook, W. S., et al. (2007). Variation in styles of rifting in the Gulf of California. *Nature*, *448*(7152), 466–469. https://doi.org/10.1038/nature06035

Lonsdale, P. (1989). Geology and tectonic history of the Gulf of California. In E. L. Winterer, D. M. Hussong, & R. W. Decker (Eds.), *The Eastern Pacific Ocean and Hawaii, Geology of North America* (pp. 499–521). Boulder, CO: Geological Society of America.

Lorenzo, J. M. (1997). Sheared continent ocean margins: An overview. *Geo-Marine Letters*, *17*(1), 1–3. https://doi.org/10.1007/PL00007201

Luth, S., Willingshofer, E., Sokoutis, D., & Cloetingh, S. (2010). Analogue modelling of continental collision: Influence of plate coupling on mantle lithosphere subduction, crustal deformation and surface topography. *Tectonophysics*, *484*(1–4), 87–102. https://doi.org/10.1016/j.tecto.2009.08.043

Martín-Barajas, A., González-Escobar, M., Fletcher, J. M., Pacheco, M., Oskin, M., & Dorsey, R. (2013). Thick deltaic sedimentation and detachment faulting delay the onset of continental rupture in the Northern Gulf of California: Analysis of seismic reflection profiles. *Tectonics*, *32*, 1294–1311. https://doi.org/10.1002/tect.20063

Mascle, J. (1976). Atlantic-type continental margins—Distinction of two basic structural types. *Anais Da Academia Brasileira De Ciencias*, *48*, 191–197.

Mauduit, T., & Dauteuil, O. (1996). Small-scale models of oceanic transform zones. *Journal of Geophysical Research*, *101*(B9), 20,195–20,209. https://doi.org/10.1029/96JB01509

Mercier de Lépinay, M., Loncke, L., Basile, C., Roest, W. R., Patriat, M., Maillard, A., & de Clarens, P. (2016). Transform continental margins—part 2: A worldwide review. *Tectonophysics*, *693*, 96–115. https://doi.org/10.1016/j.tecto.2016.05.038

Nemcok, M., Rybár, S., Sinha, S. T., Hermeston, S. A., & Ledvényiová, L. (2016). Transform margins: Development, controls and petroleum systems—An introduction. *Geological Society, London, Special Publications*, *431*(1), 1–38. https://doi.org/10.1144/SP431.15

Peace, A., McCaffrey, K. J. W., Imber, J., van Hunen, J., Hobbs, R. W., & Wilson, R. (2017). The role of pre-existing structures during rifting, continental breakup and transform system development, offshore West Greenland. *Basin Research*, *30*(3). https://doi.org/10.1111/bre.12257

Persaud, P., Di Luccio, F., & Clayton, R. W. (2015). Rayleigh wave dispersion measurements reveal low-velocity zones beneath the new crust in the Gulf of California. *Geophysical Research Letters*, *42*, 1766–1774. https://doi.org/10.1002/2015GL063420

Persaud, P., Stock, J. M., Steckler, M. S., Martín-Barajas, A., Diebold, J. B., González-Fernández, A., & Mountain, G. S. (2003). Active deformation and shallow structure of the Wagner, Consag, and Delfín basins, Northern Gulf of California, Mexico. *Journal of Geophysical Research*, *108*(B7), 2355. https://doi.org/10.1029/2002JB001937

Persaud, P., Tan, E., Contreras, J., & Lavier, L. (2017). A bottom-driven mechanism for distributed faulting in the Gulf of California rift. *Tectonophysics*, *719-720*, 51–65. https://doi.org/10.1016/j.tecto.2016.11.024

Phethean, J. J. J., Kalnins, L. M., van Hunen, J., Biffi, P. G., Davies, R. J., & McCaffrey, K. J. W. (2016). Madagascar's escape from Africa: A high-resolution plate reconstruction for the Western Somali Basin and implications for supercontinent dispersal. *Geochemistry, Geophysics, Geosystems*, *17*, 5036–5055. https://doi.org/10.1002/2016GC006624

Philippon, M., Willingshofer, E., Sokoutis, D., Corti, G., Sani, F., Bonini, M., & Cloetingh, S. (2015). Slip re-orientation in oblique rifts. *Geology*, *43*(2), 147–150. https://doi.org/10.1130/G36208.1

Ramberg, H. (1981). Gravity, deformation, and the Earth's crust. In *Theory, experiments, and geological application* (452 pp.). Cambridge, MA: Academic Press.

Reeves, C. V., Teasdale, J. P., & Mahanjane, E. S. (2016). Insight into the Eastern Margin of Africa from a new tectonic model of the Indian Ocean. *Geological Society, London, Special Publications*, *431*(1), 299. https://doi.org/10.1144/SP431.12

Reid, D. I., & Jackson, H. R. (1997). A review of three transform margins off eastern Canada. *Geo-Marine Letters*, *17*(1), 87–93. https://doi.org/10.1007/s003670050012

Rodriguez, M., Huchon, P., Chamot-Rooke, N., Fournier, M., Delescluse, M., & François, T. (2016). Tracking the paleogene India-Arabia plate boundary. *Marine and Petroleum Geology*, *72*, 336–358. https://doi.org/10.1016/j.marpetgeo.2016.02.019

Sauter, D., Ringenbach, J. C., Cannat, M., Maurin, T., Manatschal, G., & McDermott, K. G. (2018). Intraplate deformation of oceanic crust in the West Somali Basin: Insights from long-offset reflection seismic data. *Tectonics*, *37*, 588–603. https://doi.org/10.1002/2017TC004700

Sauter, D., Unternehr, P., Manatschal, G., Tugend, J., Cannat, M., le Quellec, P., et al. (2016). Evidence for magma entrapment below oceanic crust from deep seismic reflections in the Western Somali Basin. *Geology*, *44*(6), 407–410. https://doi.org/10.1130/G37747.1

Schellart, W. P., & Strak, V. (2016). A review of analogue modelling of geodynamic processes: Approaches, scaling, materials and quantification, with an application to subduction experiments. *Journal of Geodynamics*, *100*, 7–32. https://doi.org/10.1016/j.jog.2016.03.009

Schettino, A. (2015). Plate motions. In A. Schettino (Ed.), *Quantitative plate tectonics: Physics of the Earth—Plate kinematics & geodynamics* (pp. 29–80). Cham: Springer International Publishing. https://doi.org/10.1007/978-3-319-09135-8_2

Schiffer, C., Peace, A., Phethean, J., Gernigon, L., McCaffrey, K., Petersen, K. D., & Foulger, G. (2018). The Jan Mayen microplate complex and the Wilson cycle. *Geological Society, London, Special Publications*, *470*, SP470.2. https://doi.org/10.1144/SP470.2

Scrutton, R. A. (1979). On sheared passive continental margins. *Tectonophysics*, *59*(1-4), 293–305. https://doi.org/10.1016/0040-1951(79)90051-9

Seiler, C., Gleadow, A. J. W., Fletcher, J. M., & Kohn, B. P. (2009). Thermal evolution of a sheared continental margin: Insights from the Ballenas transform in Baja California, Mexico. *Earth and Planetary Science Letters*, *285*(1–2), 61–74. https://doi.org/10.1016/j.epsl.2009.05.043

Sokoutis, D., Burg, J., Bonini, M., Corti, G., & Cloetingh, S. (2005). Lithospheric-scale structures from the perspective of analogue continental collision. *Tectonophysics*, *406*(1–2), 1–15. https://doi.org/10.1016/j.tecto.2005.05.025

Stagg, H. M. J., Alcock, M. B., Bernardel, G., Moore, A. M. G., Symonds, P. A., & Exon, N. F. (2004). Geological framework of the outer Exmouth Plateau and adjacent ocean basins. (Geoscience Australia Record 2004/13).

Stock, J., Mountain, G., Diebold, J., Steckler, M. & Martin-Barajas A. (2015). HiRes multi-channel seismic shot data from the Northern Gulf of California acquired during the R/V Francisco de Ulloa expedition UL9905 (1999). Integrated Earth Data Applications (IEDA). https://doi.org/10.1594/IEDA/303735

Talwani, M., & Eldholm, O. (1973). Boundary between continental and oceanic crust at the margin of rifted continents. *Nature*, *241*(5388), 325–330. https://doi.org/10.1038/241325a0

Tchalenko, J. S. (1970). Similarities between shear zones of different magnitudes. *GSA Bulletin*, *81*(6), 1625–1940. https://doi.org/10.1130/0016-7606(1970)81[1625:SBSZOD]2.0.CO;2

Tron, V., & Brun, J. (1991). Experiments on oblique rifting in brittle-ductile systems. *Tectonophysics*, *188*(1–2), 71–84. https://doi.org/10.1016/0040-1951(91)90315-J

Tuck-Martin, A., Adam, J., & Eagles, G. (2018). New plate kinematic model and tectono-stratigraphic history of the East African and west Madagascan margins. *Basin Research*, *30*(6), 1118–1140. https://doi.org/10.1111/bre.12294

Turcotte, D. L. (1974). Are transform faults thermal contraction cracks? *Journal of Geophysical Research*, *79*(17), 2573–2577. https://doi.org/10.1029/JB079i017p02573

Vendeville, B., Cobbold, P. R., Davy, P., Choukroune, P., & Brun, J. P. (1987). Physical models of extensional tectonics at various scales. *Geological Society, London, Special Publications*, *28*(1), 95. https://doi.org/10.1144/GSL.SP.1987.028.01.08

Weijermars, R. (1986a). Flow behaviour and physical chemistry of bouncing putties and related polymers in view of tectonic laboratory applications. *Tectonophysics*, *124*(3–4), 325–358. https://doi.org/10.1016/0040-1951(86)90208-8

Weijermars, R. (1986b). Polydimethylsiloxane flow defined for experiments in fluid dynamics. *Applied Physics Letters*, *48*(2), 109–111. https://doi.org/10.1063/1.97008

Weijermars, R. (1986c). Finite strain of laminar flows can be visualized in SGM 36-polymer. *Naturwissenschaften*, *73*(1), 33–34. https://doi.org/10.1007/BF01168803

Whittaker, J. M., Williams, S. E., Halpin, J. A., Wild, T. J., Stilwell, J. D., Jourdan, F., & Daczko, N. R. (2016). Eastern Indian Ocean microcontinent formation driven by plate motion changes. *Earth and Planetary Science Letters*, *454*, 203–212. https://doi.org/10.1016/j.epsl.2016.09.019

van Wijk, J., Axen, G., & Abera, R. (2017). Initiation, evolution and extinction of pull-apart basins: Implications for opening of the Gulf of California. *Tectonophysics*, *719*, 37–50. https://doi.org/10.1016/j.tecto.2017.04.019

Wilson, J. T. (1965). A new class of faults and their bearing on continental drift. *Nature*, *207*(4995), 343–347. https://doi.org/10.1038/207343a0

Zwaan, F., & Schreurs, G. (2017). How oblique extension and structural inheritance influence rift segment interaction: Insights from 4D analog models. *Interpretation*, *5*(1), SD119–SD138. https://doi.org/10.1190/INT-2016-0063.1